PAPER

Check for updates

Significant enhancement of ferromagnetism above room temperature in epitaxial 2D van der Waals ferromagnet Fe₅₋δGeTe₂/Bi₂Te₃ heterostructures†

E. Georgopoulou-Kotsaki, [ID] *[a,b] P. Pappas, [ID] [a] A. Lintzeris, [ID] [a,c] P. Tsipas,[a]
S. Fragkos, [ID] [a,d] A. Markou,[e] C. Felser,[e] E. Longo, [ID] [f] M. Fanciulli, [ID] [g]
R. Mantovan, [ID] [f] F. Mahfouzi,[h] N. Kioussis [ID] [h] and A. Dimoulas[a]

Two-dimensional (2D) van der Waals (vdW) ferromagnetic metals Fe_xGeTe_2 with x = 3−5 have raised significant interest in the scientific community. Fe_5GeTe_2 shows prospects for spintronic applications since the Curie temperature T_c has been reported near or higher than 300 K. In the present work, epitaxial $Fe_{5-\delta}GeTe_2$ (FGT) heterostructures were grown by Molecular Beam Epitaxy (MBE) on insulating crystalline substrates. The FGT films were combined with Bi_2Te_3 topological insulator (TI) aiming to investigate the possible beneficial effect of the TI on the magnetic properties of FGT. FGT/Bi_2Te_3 films were compared to FGT capped only with AlO_x to prevent oxidation. SQUID and MOKE measurements revealed that the growth of Bi_2Te_3 TI on FGT films significantly enhances the saturation magnetization of FGT as well as the T_c well above room temperature (RT) reaching record values of 570 K. First-principles calculations predict a shift of the Fermi level and an associated enhancement of the majority spin (primarily) as well as the total density of states at the Fermi level suggesting that effective doping of FGT from Bi_2Te_3 could explain the enhancement of ferromagnetism in FGT. It is also predicted that strain induced stabilization of a high magnetic moment phase in FGT/Bi_2Te_3 could be an alternative explanation of magnetization and T_c enhancement. Ferromagnetic resonance measurements evidence an enhanced broadening in the FGT/Bi_2Te_3 heterostructure when compared to FGT. We obtain a large spin mixing conductance of $g_{eff}^{\uparrow\downarrow} = 4.4 \times 10^{20}$ m⁻², which demonstrates the great potential of FGT/Bi_2Te_3 systems for spin-charge conversion applications at room temperature.

Introduction

Since the discovery of graphene,[1] a large variety of 2D materials have been explored, bringing a lot of excitement to the scientific and engineering community. The advent of the atomically thin 2D van der Waals (vdW) metallic ferromagnet (FM) Fe_3GeTe_2 [2] with electrostatic gate tunable magnetic properties and near room temperature (RT) critical point (T_c) has opened new routes for spintronics. The new 2D FM exhibits strong perpendicular magnetic anisotropy (PMA) down to a single monolayer,[3] albeit with reduced T_c, as well as topologically protected spin textures known as skyrmions.[4,5] The latter are attributed to the presence of a positive interfacial Dzyaloshinskii–Moriya interaction (DMI) in ultrathin films or to the dipolar interactions in thicker films.[4] The material has also been found to be a topological nodal semimetal with a large intrinsic anomalous Hall current.[6] While the material has been mostly grown in bulk form at equilibrium[7–9] and studied using exfoliated thin flakes,[3,10,11] a number of wafer scale epitaxial thin films have been reported, mostly by molecular beam epitaxy (MBE).[12–14] Fe_3GeTe_2/Bi_2Te_3 heterostructures made by MBE exhibit T_c above RT up to 400 K in thin (~4 nm) films.[15]

The great success with the prototypical Fe_3GeTe_2, motivated researchers to explore the whole family of 2D metallic FM

[a]*National Centre for Scientific Research "Demokritos", Institute of Nanoscience and Nanotechnology, Agia Paraskevi, 15341 Athens, Greece.
E-mail: e.georgopoulou@inn.demokritos.gr*

[b]*Section of Condensed Matter Physics, Department of Physics, National and Kapodistrian University of Athens, Panepistimiopolis Zografou, 15784 Athens, Greece*

[c]*Department of Physics, National Technical University of Athens, School of Applied Mathematical and Physical Sciences, 15780 Athens, Greece*

[d]*Department of Mechanical Engineering, University of West Attica, 12241 Athens, Greece*

[e]*Max Planck Institute for Chemical Physics of Solids, 01187 Dresden, Germany*

[f]*Institute for Microelectronics and Microsystems, CNR-IMM Unit of Agrate Brianza, Via C. Olivetti 2, 20864 Agrate Brianza, Italy*

[g]*Department of Material Science, University of Milano Bicocca, Via R. Cozzi 55, Milan 20125, Italy*

[h]*Department of Physics and Astronomy, California State University Northridge, Northridge, CA 91330-8268, USA*

†Electronic supplementary information (ESI) available. See DOI: https://doi.org/10.1039/d2nr04820e

Fe_xGeTe_2 (x = 3–5).[16] The x = 5 member of this family, namely Fe_5GeTe_2 (FGT) has a unit cell which can be described as an assembly of three Fe–Ge slabs separated by vdW gap between the Te atoms and it is very interesting structure in many respects. It appears either in an inversion symmetric ($R\bar{3}m$ space group, no. 166) or a non-centrosymmetric structure ($R3m$ space group, no. 160). The former is the most common crystal structure in which there are three non-equivalent Fe positions per unit cell. The Fe(1) atoms preferentially occupy the crystal-lographic sites above or below neighboring Ge atoms in an alternating motif while it is forbidden to occupy both sites simultaneously as is also predicted by density functional theory (DFT) calculations.[17] The lower symmetry structure $R3m$ contains five different Fe sites with the Fe(1) atoms occupying sites either above or below the Ge atoms.[18] The characteristic signature of FGT structure is the $\sqrt{3} \times \sqrt{3}$ reconstruction which is associated with the Fe(1) site displacements in ref. 17 and 19 or Fe deficiencies[17] in $Fe_{5-\delta}GeTe_2$.

As a result of the complexity of the structure and its correlation with magnetic properties, a rich spectrum of magnetic order has been reported including pure ferromagnetism,[19–23] ferrimagnetism[24–27] and more exotic helimagnetic phase[17] that calls for further investigation of this material. In addition, by electron doping[24] a transition from FM to antiferromagnetic (AFM) has been observed. It has been suggested that FGT is an easy plane magnetized material.[21,22,28,29] On the other hand, weak PMA has been reported in mono and few layer flakes,[23,24,26,27] leaving the question about magnetocrystalline anisotropy in FGT widely open.

Although FGT is not considered as a strong PMA material, large magnetoresistance hysteresis at a small switching field has been reported,[30] indicating its potential for devices. Since the structure does not consist of just a single layer, FGT behaves more like a 3D ferromagnet;[23] the large number of spin pairs enhances the exchange interactions, thus the T_c of FGT is the highest among the Fe_xGeTe_2 family. To the best of our knowledge, FGT either bulk, exfoliated or epitaxial films,[17–23,25–28] present a T_c close to – or just above – RT (~332 K).[29] This makes FGT very attractive material for novel commercial spintronics.

However, operation of devices just above 300 K is marginal and there is pressing need for even higher T_c to realize high performance magnetic and spintronic devices. Moreover, most of the work on FGT has been performed using exfoliated flakes from the bulk. Real world applications though require wafer scale growth using MBE or other synthetic thin film growth methodologies.

Work in this direction has already started although still rather limited. Recent studies[31,32] have revealed that the substitution of Ge in FGT with As or Co enhances ferromagnetism. Although MBE has been successfully used for the wafer scale epitaxial growth of FGT on Al_2O_3 substrates,[19] no published data are available regarding the combination of FGT with Bi_2Te_3 topological insulator in analogy with the Fe_3GeTe_2/Bi_2Te_3 heterostructure which produced Fe_3GeTe_2 with enhanced T_c.[15] In any case, the role of Bi_2Te_3 in enhancing fer-

romagnetism in 2D vdWs ferromagnets remains unclear. Moreover, data associated the spin-charge conversion, a critical functionality for spintronic devices, are lacking.

To face the aforementioned challenges in achieving higher T_c FGT by wafer scale methods, in this work we employ MBE to fabricate FGT/Bi_2Te_3 heterostructures with two different FGT thicknesses and compare with bare FGT. We show that Bi_2Te_3 increases dramatically the saturation magnetization M_s and the Curie temperature T_c of FGT. Record-breaking value of $T_c \sim 570$ K is reported in this work using high temperature SQUID magnetometry. Using first principles calculations, we elucidate the possible role of Bi_2Te_3. More specifically, it is proposed that the proximity of Bi_2Te_3 to FGT increases the density of states at the Fermi level or, alternatively, induces tensile strain in FGT which stabilizes a high magnetic moment phase. Both mechanisms could be responsible for the observed enhancement of M_s. Also, using ferromagnetic resonance measurements, we report on large spin mixing conductance in FGT/Bi_2Te_3, which indicates that this heterostructure is prospective for charge-spin conversion applications at room temperature.

Experimental

XRD

X-ray diffraction patterns (XRD) were done with Siemens D5000 X-ray Diffractometer in Bragg Brentano geometry with Cu Kα radiation, in the 2θ range 5–80° with a step of 0.03° and an 8 s counting time per step.

EDS

EDS analysis has been carried out by using FEI Quanta Inspect Scanning Electron Microscope (SEM) equipped with an EDAX Energy-Dispersive X-ray Spectroscopy (EDS) system with a thermionic gun and a tungsten cathode, operated at 10–12 kV.

SQUID

Magnetization measurements were carried out using a Quantum Design (MPMS3 SQUID-VSM) magnetometer. In addition, the Curie temperature was measured using an oven option.

MOKE

Magneto-optical Kerr microscopy and magnetometry from EvicoMagnetics, equipped with a continuous flow LN_2 cryostat for low temperature measurements (77–320 K).

DFT

The DFT calculations were performed with the Vienna *Ab initio* Simulation Package (VASP) software.[33] The energy cutoff of 500 eV for the plane wave basis was used and the interactions between valence electrons and ionic cores were described with projector augmented waves (PAW),[34] while exchange and correlation effects were accounted for through the Perdew–Burke–Erzenhof (PBE) general-gradient approximation (GGA) functional.[35] Sampling of reciprocal space in total energy calcu-

lations was performed with the Monkhorst–Pack[36] method and the tetrahedron method[37] was employed for summations in k-space to obtain the electronic densities of states (DOS). The sizes of the k-point grids were $15 \times 15 \times 1$ for the structural relaxation and $30 \times 30 \times 1$ for electronic properties calculations. The DOS were calculated in -10 to $+10$ eV range and with 4000 points in Energy. van der Waals interactions were included through dispersion corrected DFT at the DFT-D3 level.[38] For calculations in 2D materials and slabs, a vacuum of at least 20 Å was added in the z-direction to ensure minimal interactions between adjacent images.

FMR

Broadband ferromagnetic resonance (BFMR) experiments were conducted using a home-made facility composed by a Bruker ER-200 electromagnet, an Anritsu-MG3694C radio frequency (RF) source, a Quantum Design grounded coplanar waveguide (GCPW), a Wiltron-70KB50 NEG rectifying diode and a lock-in amplifier.[39,40] During the BFMR measurement, to avoid the shortening of the electrical line, the active part of the GCPW was covered with a 75 μm thick Kapton tape and the sample was placed face down on the GCPW in the so-called "flip-chip" mode. The GCPW and the sample were positioned between the poles of the electromagnet, with the external magnetic field (H) lying parallel to the film plane in the so-called *in-plane configuration* (IP). The input port of the GCPW was connected to the RF-source and the output port to the rectifying diode to convert the transmitted rf signal into a dc current. The rectified signal was then sent to a lock in amplifier for its acquisition. To perform cavity-FMR measurements was employed the same Bruker ER-200 electromagnet adopted for BFMR. In this case the sample was placed in a standard ER 4102 ST Bruker resonating cavity. Such a resonator operates in the TE_{102} mode and X-band frequency range, with a quality factor $Q = \dfrac{f_{res}}{\Delta f}$ value of 6000.

Results and discussion

Synthesis and structural characterization

High quality FGT epitaxial films were grown by molecular beam epitaxy (MBE) on insulating substrates sapphire (0001)/WS_2 (001) and undoped $SrTiO_3$ (111) (STO). For the Fe and Ge evaporation two e-guns were used while Te was evaporated from a thermal cracker cell. Before FGT deposition, sapphire/WS_2 substrate was annealed at 450 °C and STO at 800 °C under molecular oxygen flux for 5 min. During the film growth the pressure was kept 10^{-8} Torr and the substrate temperature was set at 332 °C. The flux ratio of Fe : Ge was set on 5 : 1 and under Te overpressure. Two different series of samples were grown with 17 nm and 9 nm respectively and were capped *in situ* with 4 nm amorphous AlO_x (rate of Al: 0.1 Å s^{-1}) at RT to avoid oxidation. For both series, Bi_2Te_3 was grown on top of FGT films in order to investigate the effect of the TI. More specifically, Table 1 presents the series of films that were grown.

Table 1 The epitaxial films that were grown

Sample	Substrate	Structure	Capping
FGT	Sapphire (0001)/WS_2	$Fe_{5-\delta}GeTe_2$ (17 nm)	AlO_x
FGT/Bi_2Te_3	Sapphire (0001)/WS_2	$Fe_{5-\delta}GeTe_2$ (17 nm)	Bi_2Te_3
FGT	$SrTiO_3$	$Fe_{5-\delta}GeTe_2$ (9 nm)	AlO_x
FGT/Bi_2Te_3	$SrTiO_3$	$Fe_{5-\delta}GeTe_2$ (9 nm)	Bi_2Te_3

The samples were characterized *in situ* by reflection high energy electron diffraction (RHEED). Fig. 1 shows the RHEED patterns of the sapphire (0001)/WS_2 substrate along the two azimuthal directions of sapphire (top) and the deposited 17 nm thick FGT film (bottom). The FGT streaky pattern is rotationally aligned with the substrate, showing no evidence for 30 deg or 90 deg rotated domains, despite the large lattice mismatch, which indicates van der Waals epitaxial growth of FGT on the sapphire/WS_2 substrate. Moreover, the RHEED pattern shows a 3×1 reconstruction which is compatible with a $(\sqrt{3} \times \sqrt{3})$ R30° superstructure as seen by directly comparing the RHEED pattern with the reciprocal lattice in Fig. 1. Similar superstructure is observed in thin (9 nm) FGT grown on STO (111) substrates (see Fig. S1†). The $(\sqrt{3} \times \sqrt{3})$ R30° superstructure indicates the presence of Fe-deficient $Fe_{5-\delta}GeTe_2$ structure as previously reported.[17]

From the RHEED pattern (Fig. S2†) the lattice constant α is estimated to be 4.063 Å and 4.049 Å for the 17 nm 9 nm thick FGT, respectively which are in good agreement with literature values.[19]
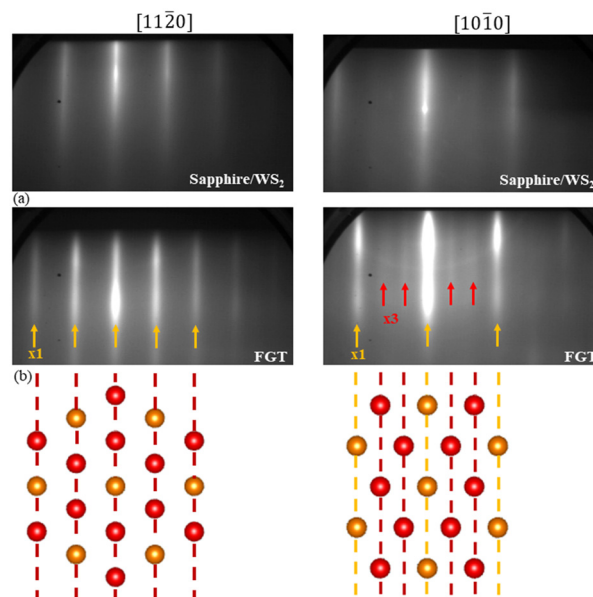

Fig. 1 RHEED diffraction patterns before and after the deposition for 17 nm thick FGT. (a) The pictures for the sapphire (0001) substrate along two perpendicular azimuths. (b) The pictures for the FGT along two perpendicular azimuths. The arrows show a 3×1 reconstruction which is compatible with a $(\sqrt{3} \times \sqrt{3})$ R30° superstructure as illustrated by the red circles in the reciprocal space diagrams below the RHEED pattern.

As mentioned above, recent reports have revealed that the tendency to form Fe deficiencies allows the synthesis of $Fe_{5-\delta}GeTe_2$ with a variety of crystal structures both centrosymmetric and noncentrosymmetric.[17,18,25]

Fig. 2(a) left panel shows the structure of noncentrosymmetric ($R3m$) $Fe_{5-\delta}GeTe_2$, whereas the right panel shows the centrosymmetric structure ($R\bar{3}m$). The main difference between the two structures is the presence of split site Fe(1) occupying sites above and below Ge alternately (centrosymmetric) or occupying a site only above Ge in the unit cell and thus break the inversion symmetry.

X-ray diffraction (XRD) patterns are shown in Fig. 2(b) and (c). The 17 nm thick FGT (Fig. 2(b)) consists of a clear Fe_5GeTe_2 lattice whereas in the FGT/Bi_2Te_3 pattern secondary weak Bragg reflections are present which are attributed to the Fe_3GeTe_2 phase. The 9 nm thick FGT film (Fig. 2(c)) shows a clear contribution from Fe_5GeTe_2 structure and for FGT/Bi_2Te_3 sample there is a small peak that can be identified as the (006) reflection of Fe_3GeTe_2, thus suggesting the presence of F_3GeTe_2 as a secondary phase. The XRD results in combination with the RHEED patterns verify that our epitaxial films contain mainly the Fe_5GeTe_2 phase. In order to verify the stoichiometry of our samples, complementary Energy Dispersive Spectroscopy (EDS) analysis was performed for 17 nm thick FGT/Bi_2Te_3 and was confirmed that is in very good agreement with the nominal stoichiometry ($x_{Fe} = 5$) (Fig. S3†).

Table 2 displays the lattice constant c as determined by the XRD patterns, for all heterostructures which is in good agreement with literature.[18,19,25,26]

Magnetic properties

MOKE magnetometry and microscopy. The samples are first imaged and measured by MOKE in the longitudinal mode. Data for the 17 nm thick FGT and FGT/Bi_2Te_3 are shown in Fig. 3.

It can be seen that for FGT capped with a protective AlO_x layer, the hysteresis loop is gradually reduced in terms of remanent magnetization and coercive field as the temperature rises and is effectively diminished after 310 K. This behavior is compatible with a T_c just above 300 K as has already been reported for this material.[17,19,21,23,26,28] In contrast, the hysteresis loop of FGT/Bi_2Te_3 is reduced mainly in terms of coercive field as the temperature rises up to 290 K and then it shows a clear tendency to remain invariant as the temperature is further raised up to 320 K, indicating that the T_c of FGT/Bi_2Te_3 could be much higher than 300 K. The same behavior is observed for the thin FGT samples as shown in supplementary (Fig. S4†). In summary, the presence of Bi_2Te_3 in the heterostructure makes FGT ferromagnetic with a well-defined hysteresis loop well above RT. The difference in the behaviour of the MOKE $M–H$ loops for bare FGT and FGT/Bi_2Te_3 is attributed to the difference in the T_c of the two materials systems. In the case of bare FGT, as the temperature approaches $T_c \sim 310$ K, the magnetization drops to zero, dramatically affecting the saturation magnetization of the hysteresis loop (Fig. 3(a)). In contrast, in the case of FGT/Bi_2Te_3, the T_c is much higher, ~570 K, (see section
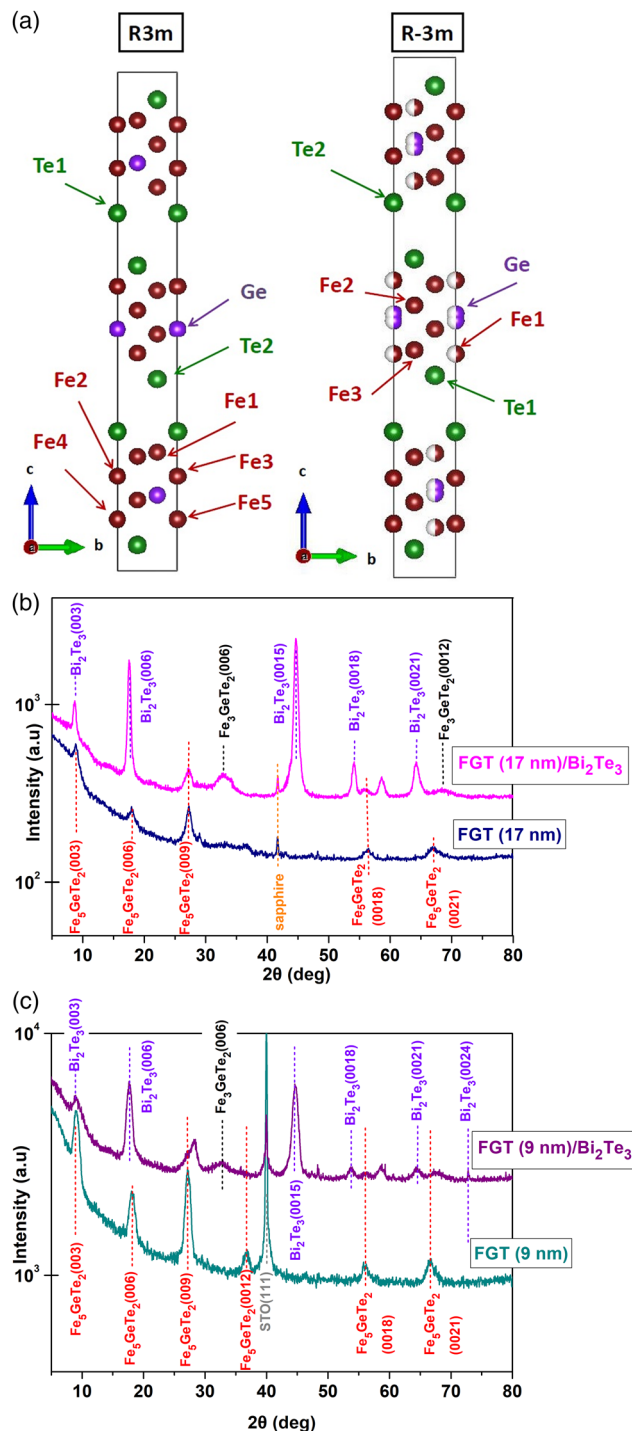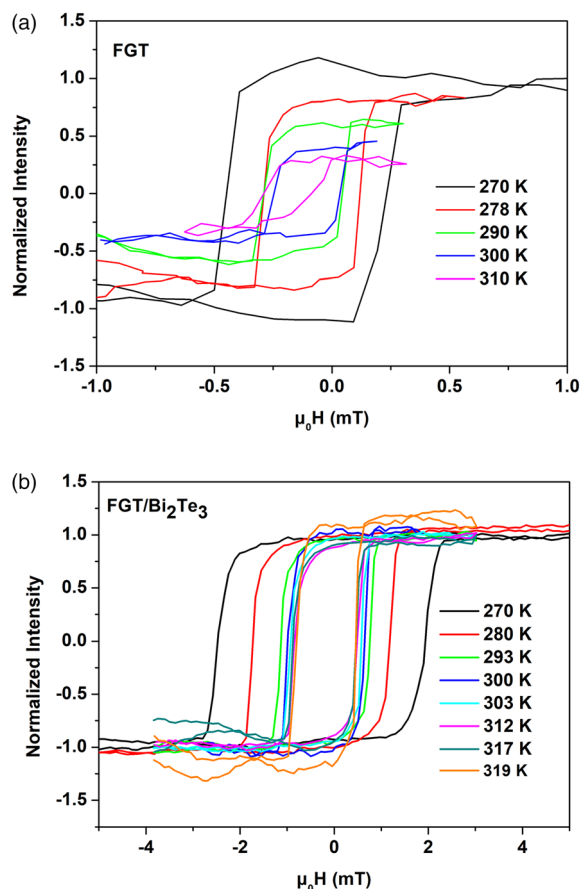

Fig. 2 (a) Crystal structure of $Fe_{5-\delta}GeTe_2$, in the left panel the unit cell of the non centrosymmetric $R3m$ structure with all nonequivalent atomic positions is depicted, the right panel presents the centrosymmetric structure $R\bar{3}m$. (b) XRD patterns for 17 nm thick FGT and FGT/Bi_2Te_3 heterostructures and (c) XRD patterns for 9 nm thick FGT and FGT/Bi_2Te_3 heterostructures compared with the expected (00l) reflections.

about SQUID magnetometry below) so the saturation magnetization varies slowly leaving the hysteresis loops essentially unaltered (Fig. 3(b)).
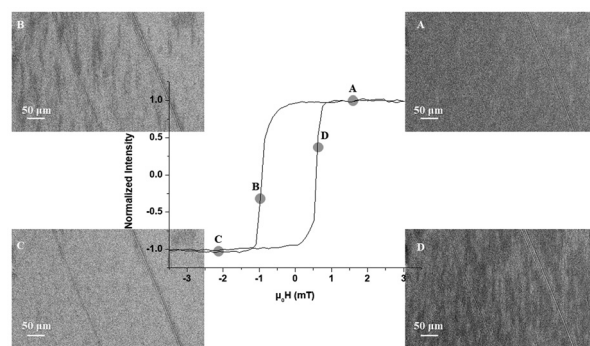
Table 2 Lattice constant c for all samples

Hetero structures	FGT (17 nm)	FGT (17 nm)/Bi$_2$Te$_3$	FGT (9 nm)	FGT (9 nm)/Bi$_2$Te$_3$
c (Å)	29.30	29.47	29.64	29.37

Fig. 3 MOKE hysteresis loops for 17 nm thick FGT (a) and FGT/Bi$_2$Te$_3$ (b) heterostructures.

It should be noted that AlO$_x$ is deposited as a capping layer to protect FGT from oxidation. AlO$_x$ is known to be non-magnetic, it has little – or no – spin orbit coupling and has no topological insulator properties; therefore, it is not expected to affect the magnetic behaviour of FGT underneath. Therefore, the MOKE hysteresis loops of FGT/AlO$_x$ are expected to be the same as in the case of an uncovered (bare) FGT which is measured under inert atmosphere conditions to prevent oxidation.

Ferromagnetic domains are also imaged under in plane (IP) magnetic field (Fig. 4). The material is first saturated at ~+300 mT and the domains show up as black and white contrast when the material is demagnetized at an opposite (coercive) field of ~−1 mT. The domains appear as elongated irregular shapes on average about 100 μm long and 10–20 μm wide. It is important to note that the domains are better visible at 77 K but they persist with a clear contrast up to 300 K (Fig. 4).

Fig. 4 MOKE Hysteresis loop and domain imaging at points 'A', 'B', 'C', 'D' on hysteresis loop, for 17 nm thick FGT/Bi$_2$Te$_3$ at 300 K.

SQUID magnetometry

While MOKE magnetometry gives a first qualitative indication about the persistence of ferromagnetism well above 300 K for the FGT/Bi$_2$Te$_3$ heterostructure with clear-cut FM loops at low fields ~few mT, the quantification in terms of saturation magnetization M_s at high fields ~6 T is performed using SQUID magnetometry (Fig. 5, and Fig. S5–S10†).

Fig. 5 shows the main $M–H$ characteristics curves for RT and the lowest attainable temperature of 20 K. The highly non-linear $M–H$ curve reveals ferromagnetism in all films which persists and is quite strong up to 300 K at least. This confirms the MOKE results that indicated FM films above RT especially for the FGT/Bi$_2$Te$_3$ heterostructure.

The data in Fig. 5 and Fig. S5–S7† show that films are rather isotropic. In the case of FGT/Bi$_2$Te$_3$ a clear IP magnetic anisotropy prevails above 200 K since the M_s is reached at lower magnetic fields (Fig. 5(b)) and a very sharp loop is observed at RT in conjunction with MOKE data.

Fig. 6 shows the normalized (in units emu cm^{-2}) saturation magnetization M_s as a function of temperature extracted from the $M–H$ curves. The M_s for all samples increases with decreasing temperature showing typical behavior for ferromagnetic ordering.

The two FGT samples with different thickness (black and red squares in Fig. 6(a)) show very similar IP normalized M_s behavior as expected. On the other hand, the two FGT/Bi$_2$Te$_3$ heterostructures (black and red circles in Fig. 6(a)) show enhanced IP M_s which is attributed to the beneficial influence of the Bi$_2$Te$_3$ layer. It is important to note that this influence is more pronounced in the case of the thinner sample (9 nm) where the enhancement reaches 148% compared to the case of the thicker sample (17 nm) where the enhancement is estimated to be 83% at RT. It is anticipated that Bi$_2$Te$_3$ TI results in electron doping of FGT originating from the topological surface states. Then, the bigger influence on the thinner sample is expected the region close to the interface represents a bigger portion of the total FGT volume. Similar behavior is observed for the OP M_s presented in Fig. 6(b).

The data in Fig. 6 suggest that the FGT/Bi$_2$Te$_3$ heterostructures are expected to have a larger T_c compared to the
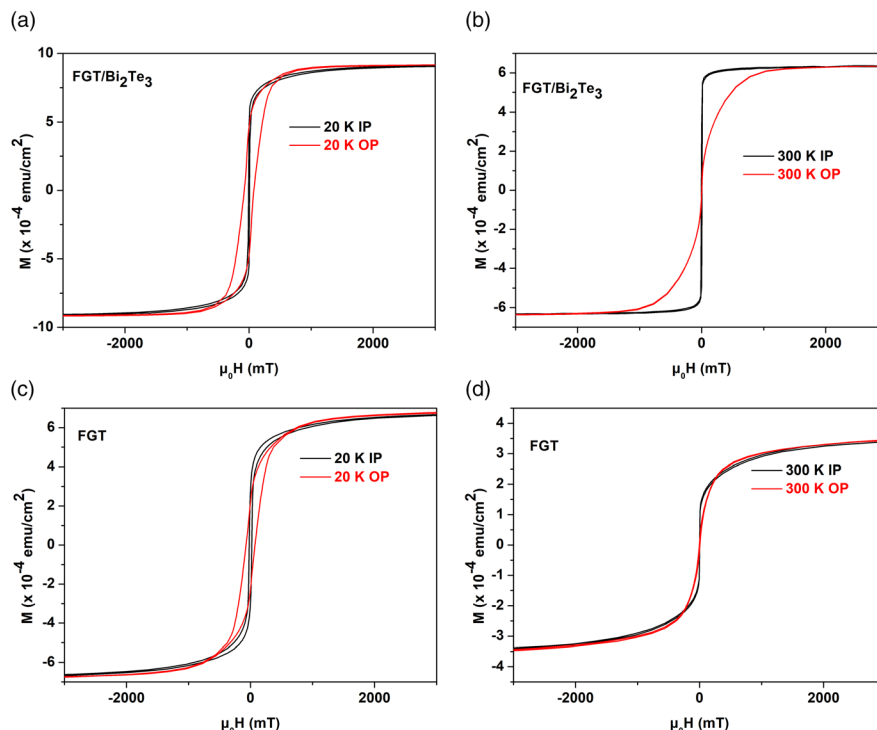
Fig. 5 Comparison of in plane (IP) and out of plane (OP) component by SQUID measurements for 17 nm thick FGT/Bi_2Te_3 (a and b) and FGT (c and d).

FGT, which could be significantly larger than 300 K. In order to accurately determine the T_c, an evacuated furnace has been used to cover the temperature range 300–620 K and the normalized $M_s - T$ results are shown in Fig. 7 for one of our FGT/Bi_2Te_3 heterostructures with FGT thickness of 17 nm.

It can be inferred that the T_c is around 570 K which, to the best of our knowledge, is the highest reported to literature values.

In summary, from our magnetic measurements can be concluded that for the 17 nm thick FGT sample the presence of the TI helps retaining the FM order at elevated temperatures shifts the T_c significantly above RT and stabilizes an IP nonzero magnetization in the high temperature range, in contrast to the FGT which exhibits a more isotropic behavior with a significantly smaller magnetization, becoming almost negligible above RT.

First principles calculations

To better understand the beneficial effect of Bi_2Te_3 on the FM properties of Fe_5GeTe_2, *ab initio* Density Functional Theory (DFT) calculations[33] were performed for the two cases of FGT and FGT/Bi_2Te_3, as described in the Experimental section. Additional details of the calculations can be found in Fig. S11.†

The calculated spin-resolved energy density of states (DOS) of FGT (Fig. S12(a)†) is compared to that of FGT/Bi_2Te_3 (Fig. S12(b)†) heterostructure. They have the expected DOS of itinerant ferromagnet with sharp features similar to those reported in ref. 41. When the DOS is plotted in a limited range

around the Fermi energy, a twofold effect is observed (Fig. 8). First, near the Fermi level there is an increase in the overall DOS of FGT/Bi_2Te_3 due to the contribution of Bi and Te orbitals *via* proximity (Fig. S13†). Second, there is an energy shift of the Fermi level of FGT/Bi_2Te_3 compared to the FGT monolayer. Noting that the Fermi level is kept at $E = 0$ by convention, it can be seen from Fig. 8 that the Fermi level moves from just below the peak indicated by arrows in FGT to above the same peak in FGT/Bi_2Te_3. As a result, the majority spin $(D(E_F)_\uparrow)$ density of states for the two layers (FGT and FGT/Bi_2Te_3) differ significantly at the Fermi level in favor of FGT/Bi_2Te_3. The combined effect of the two, results in a significant increase by 28% of the FGT/Bi_2Te_3 total density of states D (E_F) compared to FGT. Within the Stoner approximation for itinerant ferromagnets an enhancement of D (E_F) is associated with an increase in magnetization as observed in the experiment (Fig. 6).

In a mean field approximation, an increase of saturation magnetization is accompanied by an increase in the T_c as observed in Fig. 7. This is in line with previous report[42] that femtosecond laser pulses induced doping can modify the electronic band structure of Fe_3GeTe_2 enhancing M_s and T_c from 250 to 300 K. Similarly, MBE grown 4 ML Fe_3GeTe_2 exhibits enhanced T_c up to 400 K when it is in contact with Bi_2Te_3 attributed to increased carrier doping of Fe_3GeTe_2 induced by Bi_2Te_3.[15] Finally, effective electrostatic doping has been considered responsible for the increase of Fe_3GeTe_2 T_c from 225 K to RT.[2]

Alternatively, the significant increase of the total magnetic moment in the present of Bi_2Te (Fig. 6), suggests the presence
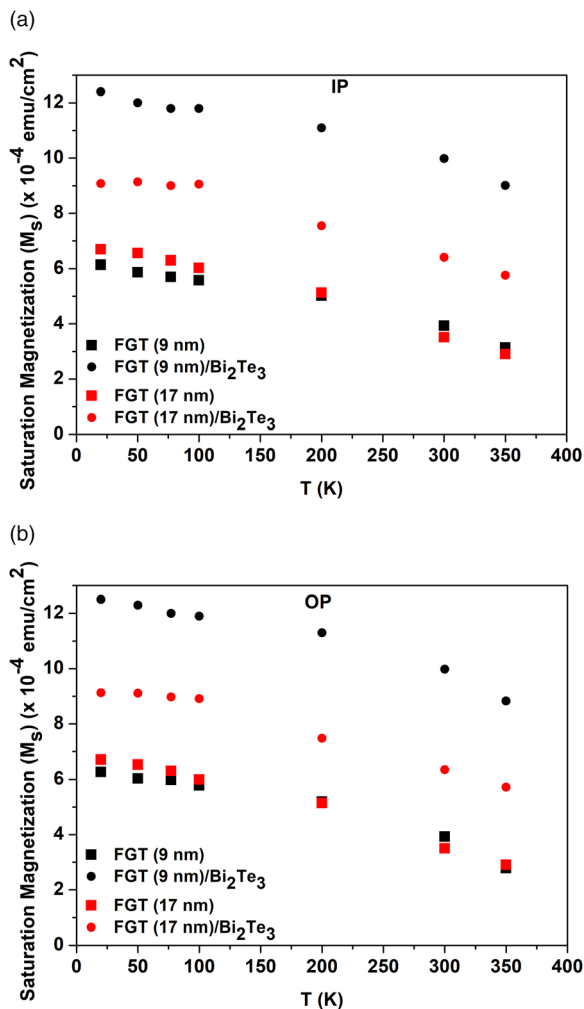
(a)

(b)

Fig. 6 Temperature dependence of saturation magnetization M_s measured by SQUID for all the samples for the in plane (IP) component (a), out of plane (OP) component (b).

(a)

(b)

Fig. 7 Temperature dependence of the Normalized magnetization for 17 nm thick FGT/Bi$_2$Te$_3$ (a) in the temperature range 5 K–400 K with normalization $M - M_{400\ K}/(M_{5\ K} - M_{400\ K})$ and (b) in the temperature range 300 K–620 K with normalization $M - M_{620\ K}/(M_{300\ K} - M_{620\ K})$.

of multiple (two) magnetic phases in FGT, whereby, the change of chemical environment in the presence of the Bi$_2$Te$_3$ can favor one phase over the other. Recent *ab initio* calculations of the FGT monolayer predicted a significant enhancement of the total magnetic moment under an in-plane tensile strain.[43] The lattice constant mismatch of more than 10% between FGT (4.05 Å) and Bi$_3$Te$_2$ (4.5 Å) indicates the presence of a tensile strain on the FGT layers at the interface region. We have carried out *ab initio* electronic structure calculations using the Vienna *ab initio* Simulation Package (VASP)[33] to investigate the effect of strain on the magnetic properties of bulk FGT. In Fig. 9(a) we show the calculated total energy *versus* the constrained total magnetic moment for bulk FGT under 2% and 5% in-plane tensile strain denoted by the dashed-blue and solid-red curves, respectively. In the case of 2% tensile strain (blue dash-dotted curve), the results predict the coexistence of the two magnetic phases as they are energetically degenerate and separated by a relatively small energy barrier height of about 6 meV. As the tensile strain increases to
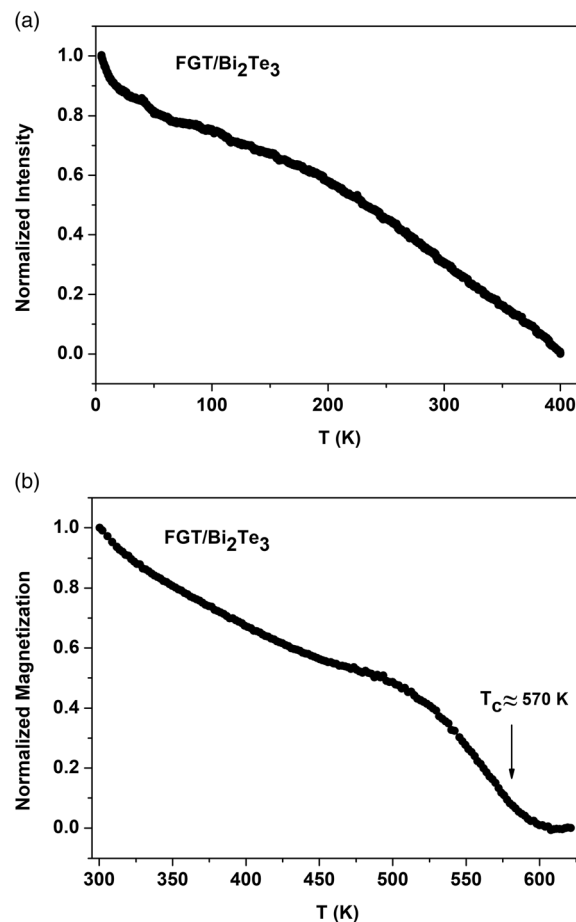
5% (red curve in Fig. 9(a)), the high magnetic moment (11.2μ_B) phase is stabilized showing a total energy minimum. In Fig. 9(b) we plot the total magnetic moment *versus* applied tensile strain which shows a phase transition at about 2.5% strain. The atom-resolved magnetic moments, shown in Fig. 9(c), demonstrate that the enhancement of the magnetic moment is primarily due to emergence of magnetization in Fe$_5$ atom under strain. This enhancement explains the larger saturation magnetization values M_s observed in FGT/Bi$_2$Te$_3$ heterostructures by SQUID magnetometry.

Spin accumulation at the FGT/Bi$_2$Te$_3$ interface

In order to investigate the role of interfacing FGT with Bi$_2$Te$_3$ on its magnetization dynamics, we conducted cavity ferromagnetic resonance (FMR) at 9.78 GHz (ref. 44 and 45) (see Experimental, Fig. S14†), on both FGT and FGT/Bi$_2$Te$_3$ samples. The results are depicted in Fig. 10, with empty black squares (full blue squares) representing the FGT (FGT/Bi$_2$Te$_3$) samples. In particular we investigated the systems with 9 nm FGT layers.

From the fit of the two curves, we can extract the resonance field (H_{res}) and the signal's linewidth (ΔH). The results are
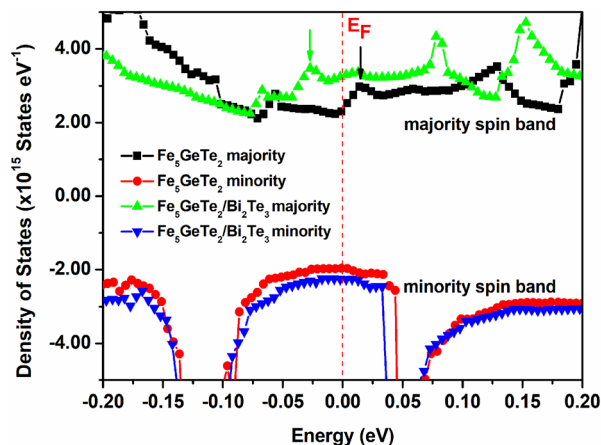
Fig. 8 Calculated spin resolved density of states close to the Fermi level of FGT (black and red lines and closed symbols) and FGT/Bi$_2$Te$_3$ (green and blue lines and closed symbols). The red dashed line indicates the Fermi level placed by convention at zero energy. The green and black arrows indicate the two different energy positions of a characteristic peak in the majority spin DOS that helps visualizing the energy shift of the Fermi level: for FGT, the Fermi level is below, while for FGT/Bi$_2$Te$_3$ it is above the peak.
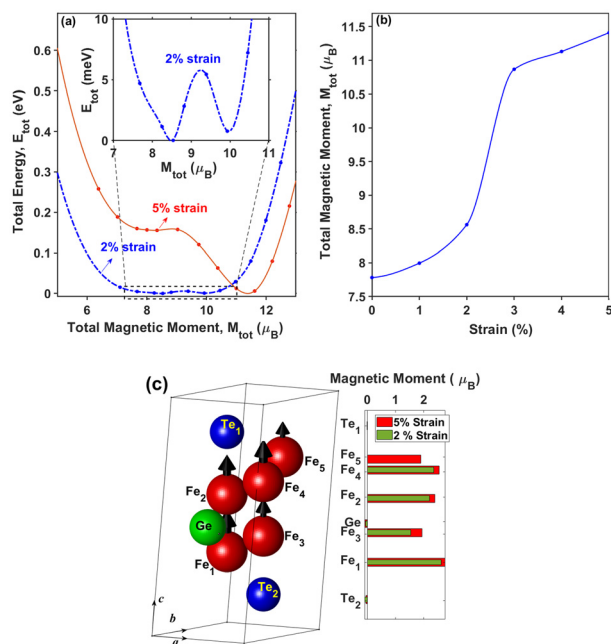

Fig. 9 (a) Calculated total energy *versus* constrained total magnetic moment in bulk Fe$_5$GeTe$_2$ under 2% and 5% tensile inplane strain. Inset shows a magnification in the low-energy region (for $7\mu_B < M_{tot} < 11\mu_B$) under 2% strain. (b) Total magnetic moment *versus* applied tensile inplane strain. (c) Crystal structure and the corresponding values of the atom-resolved magnetic moments.

H_{res}^{FGT} = 2082 ± 0.8 Oe and ΔH^{FGT} = 511 ± 2 Oe for the FGT sample, and H_{res}^{FGT/Bi_2Te_3} = 2259 ± 5 Oe and $\Delta H^{FGT/Bi_2Te_3}$ = 965 ± 12 Oe for the FGT/Bi$_2$Te$_3$ sample. We detect a clear enhancement of the ΔH in the FGT/Bi$_2$Te$_3$ sample. This is associated
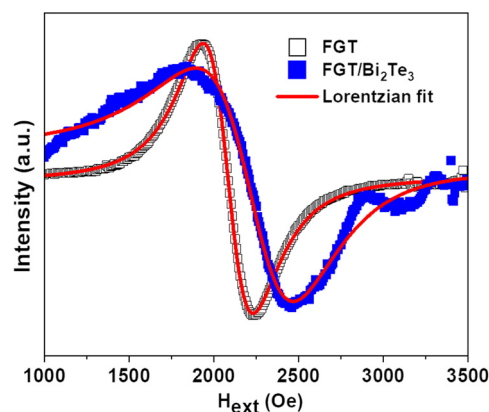

Fig. 10 Comparison of the FMR signals for the FGT (empty black squares) and FGT/Bi$_2$Te$_3$ (full blue squares) samples acquired by resonant cavity FMR at 9.78 GHz.

to an enhancement of the damping parameter α, since these quantities are correlated as depicted in eqn (1).

$$\Delta H = \Delta H_0 + \frac{4\pi}{|\gamma|}\alpha f_{res} \qquad (1)$$

Indeed, according to eqn (1), by assuming ΔH_0 equal for both samples, we can write $\Delta H^{FGT/Bi_2Te_3} - \Delta H^{FGT} = \frac{4\pi}{|\gamma|}f_{res}(\alpha^{FGT/Bi_2Te_3} - \alpha^{FGT})$.

In the framework of the spin pumping model, the enhancement of α is related to the generation of pure spin currents in a ferromagnetic layer.[46,47] Indeed, these phenomena are already reported for several chalcogenide-based TIs (*i.e.* Sb$_2$Te$_3$, B$_2$Se$_3$, Bi$_2$Te$_3$).[40,48,49]

Our results show that Bi$_2$Te$_3$ acts as a good spin sinking material when in contact with FGT, with the spin current that is generated at resonance within the FGT layer being markedly absorbed by the neighboring Bi$_2$Te$_3$. This process can be quantified by calculating the so called *spin mixing conductance* $G_{eff}^{\uparrow\downarrow}$, an intrinsic property of a system whose real part is proportional to the amount of the spin current crossing the FGT/Bi$_2$Te$_3$ interface and absorbed by the spin sink layer, as regulated by eqn (2).

$$\begin{aligned}
\text{Re}(G_{eff}^{\uparrow\downarrow}) = g_{eff}^{\uparrow\downarrow} &= \frac{4\pi M_s t_{FM}}{g\mu_B}(\alpha_{S2} - \alpha_{S1}) \\
&= \frac{2M_s t_{FM}\gamma}{g\mu_B f}\left(\Delta H^{FGT/Bi_2Te_3} - \Delta H^{FGT}\right)
\end{aligned} \qquad (2)$$

Considering f = 9.78 GHz, the γ and g-factor values extracted from broadband FMR (see ESI†), and the M_s^{FGT/Bi_2Te_3} = 1108 emu cm^{-3} extracted from SQUID at 300 K by assuming a FGT thickness of 9 nm (see Fig. 6), from eqn (2), we calculate $g_{eff}^{\uparrow\downarrow}$ = 4.4 × 10^{20} m^{-2}.

It is of interest to compare the $g_{eff}^{\uparrow\downarrow}$ we obtain in the FGT/Bi$_2$Te$_3$ system, with those reported for the Bi$_2$Te$_3$ and others topological insulators in contact with traditional ferromagnets. Indeed, the Table 1 of ref. 40 shows how the latter value is higher than most of those found in literature for similar

systems. More specifically, F. B. Abdulahad *et al.*[49] used FMR to probe a NiFe/Bi$_2$Te$_3$ heterostructure, reporting a $g_{\text{eff}}^{\uparrow\downarrow}$ in the 1–4×10^{19} m^{-2} range, being one order of magnitude lower than the $g_{\text{eff}}^{\uparrow\downarrow}$ value we measure in FGT/Bi$_2$Te$_3$.

Our results demonstrate the great potential of the developed FGT/Bi$_2$Te$_3$ system towards its use as an efficient spin-charge converter based on the 2D ferromagnet Fe$_{5-\delta}$GeTe$_2$ and the 3D topological insulator Bi$_2$Te$_3$.

Conclusions

In this work, Fe$_{5-\delta}$GeTe$_2$ (FGT) and FGT/Bi$_2$Te$_3$ heterostructures were grown epitaxially by MBE on crystalline substrates. Two different thicknesses (9 and 17 nm) of FGT films were investigated. The structural quality and composition of films were verified by *in situ* RHEED and XRD. A ($\sqrt{3} \times \sqrt{3}$) R30° phase observed in RHEED is characteristic of a sub-stoichiometric Fe$_{5-\delta}$GeTe$_2$ material. The presence of this phase was also confirmed by XRD.

MOKE in the longitudinal mode near RT reveals that FGT/Bi$_2$Te$_3$ heterostructures are ferromagnetic with a clear IP *M–H* ferromagnetic loop which remains robust for temperatures well above 300 K indicating a high T_c. This is in contrast to the case of FGT which shows a fast-reducing *M–H* loop near RT indicating a T_c close to-or just above 300 K. The enhancement of T_c in FGT/Bi$_2$Te$_3$ is verified by high temperature SQUID measurements in a furnace for a 17 nm FGT/Bi$_2$Te$_3$ sample which shows T_c as high as 570 K. Moreover, a systematic investigation by SQUID shows that the FGT/Bi$_2$Te$_3$ has an enhanced M_s compared to FGT at all temperature range below 350 K, which becomes more pronounced in the thinner samples. First principles calculations predict a contribution to the total DOS of Bi and Te due to proximity as well as a Fermi level shift influenced by the proximity to the Bi$_2$Te$_3$ layer, both of which favor a larger total DOS for the FGT/Bi$_2$Te$_3$ compared to FGT. In the framework of a Stoner approximation for an itinerant ferromagnet, such an increase of the DOS could explain the observed enhancement in M_s and T_c and the overall strengthening of ferromagnetism in the case of FGT/Bi$_2$Te$_3$ in line with the experiments. Alternatively, the stabilization of a high magnetic moment state in the presence of >2% tensile strain, likely originating from the lattice mismatch between FGT and Bi$_2$Te$_3$, as predicted by DFT calculations, could explain, at least partly, the magnetization enhancement. Finally, the FGT and FGT/Bi$_2$Te$_3$ heterostructure were probed by ferromagnetic resonance, with a revealed enhancement of damping parameter for FGT/Bi$_2$Te$_3$ when compared to FGT, suggesting the suitability of such an heterostructure to exploit spin-charge conversion effects in spintronic devices based on 2D ferromagnets and 3D topological insulators.

Author contributions

E. Georgopoulou-Kotsaki was involved in the conceptualization, investigation of MOKE and structural characteriz-

ation data as well as the writing, visualization and editing of the original draft. Dr P. Pappas was involved in the conceptualization, investigation of MOKE data, DFT calculations, as well as the writing and reviewing of the draft. A. Lintzeris was involved in the conceptualization and the acquisition of MOKE data. Dr P. Tsipas was involved in the materials fabrication. S. Fragkos was involved in DFT calculations. A. Markou and C. Felser were involved in investigation of SQUID measurements as well as editing and reviewing of the draft. E. Longo and R. Mantovan were involved in the investigation of FMR data as well as editing and reviewing of the draft. M. Fanciulli was involved in editing and reviewing of the draft. F. Mahfouzi and N. Kioussis were involved in DFT calculations as well as editing and reviewing of the draft. A. Dimoulas was involved in the project supervision and validation as well as editing and reviewing of the draft.

Conflicts of interest

There are no conflicts to declare.

Acknowledgements

References

1 K. S. Novoselov, A. K. Geim, S. V. Morozov, D. Jiang, Y. Zhang, S. V. Dubonos, I. V. Grigorieva and A. A. Firsov, Electric Field Effect in Atomically Thin Carbon Films, *Science*, 2004, **306**, 666–669.

2 Y. Deng, Y. Yu, Y. Song, J. Zhang, N. Z. Wang, Z. Sun, Y. Yi, Y. Z. Wu, S. Wu, J. Zhu, J. Wang, X. H. Chen and Y. Zhang, Gate tunable room-temperature ferromagnetism in two-dimensional Fe3GeTe2, *Nature*, 2018, **563**, 94–99.

3 Z. Fei, B. Huang, P. Malinowski, W. Wang, T. Song, J. Sanchez, W. Yao, D. Xiao, X. Zhu, A. F. May, W. Wu, D. H. Cobden, J.-H. Chu and X. Xu, Two-dimensional itinerant ferromagnetism in atomically thin Fe3GeTe2, *Nat. Mater.*, 2018, **17**, 778–782.

4 B. Ding, Z. Li, G. Xu, H. Li, Z. Hou, E. Liu, X. Xi, F. Xu, Y. Yao and W. Wang, Observation of Magnetic Skyrmion Bubbles in a van der Waals Ferromagnet Fe3GeTe2, *Nano Lett.*, 2020, **20**, 868–873.

5 Y. Wu, S. Zhang, J. Zhang, W. Wang, Y. L. Zhu, J. Hu, G. Yin, K. Wong, C. Fang, C. Wan, X. Han, Q. Shao, T. Taniguchi, K. Watanabe, J. Zang, Z. Mao, X. Zhang and K. L. Wang, Néel-type skyrmion in WTe2/Fe3GeTe2 van der Waals heterostructure, *Nat. Commun.*, 2020, **11**, 3860.

6 K. Kim, J. Seo, E. Lee, K.-T. Ko, B. Kim, B. G. Jang, J. M. Ok, J. Lee, Y. J. Jo, W. Kang, J. H. Shim, C. Kim, H. W. Yeom, B. I. Min, B.-J. Yang and J. S. Kim, Large Anomalous Hall current induced by topological nodal lines in a ferromagnetic van der Waals semimetal, *Nat. Mater.*, 2018, **17**, 794–799.

7 H.-J. Deiseroth, K. Aleksandrov, C. Reiner, L. Kienle and R. K. Kremer, Fe3GeTe2 and Ni3GeTe2 – Two New Layered Transition-Metal Compounds: Crystal Structures, HRTEM Investigations, and Magnetic and Electrical Properties, *Eur. J. Inorg. Chem.*, 2006, **8**, 156.

8 B. Chen, J. Yang, H. Wang, M. Imai, H. Ohta, C. Michioka, K. Yoshimura and M. Fang, Magnetic Properties of Layered Itinerant Electron Ferromagnet Fe3GeTe2, *J. Phys. Soc. Jpn.*, 2013, **82**(12), 124711.

9 Y. Zhang, H. Lu, X. Zhu, S. Tan, W. Feng, Q. Liu, W. Zhang, Q. Chen, Y. Liu, X. Luo, D. Xie, L. Luo, Z. Zhang and X. Lai, Emergence of Kondo lattice behavior in a van der Waals itinerant ferromagnet Fe3GeTe2, *Sci. Adv.*, 2018, **4**, eaao6791.

10 Q. Li, M. Yang, C. Gong, R. Chopdekar, A. N'Diaye, J. Turner, G. Chen, A. Scholl, P. Shafer, E. Arenholz, A. K. Schmid, S. Wang, K. Liu, N. Gao, A. S. Admasu, S. W. Cheong, C. Hwang, J. Li, F. Wang, X. Zhang and Z. Qiu, Patterning-Induced Ferromagnet of Fe3GeTe2 van der Waals Materials beyond Room Temperature, *Nano Lett.*, 2018, **18**(9), 5974–5980.

11 C. Tan, J. Lee, S.-G. Jung, T. Park, S. Albarakati, J. Partridge, M. R. Field, D. G. McCulloch, L. Wang and C. Lee, Hard magnetic properties in nanoflake van der Waals Fe3GeTe2, *Nat. Commun.*, 2018, **9**, 1–7.

12 J. M. J. Lopes, D. Czubak, E. Zallo, A. I. Figueroa, C. Guillemard, M. Valvidares, J. Rubio-Zuazo, J. López-Sanchéz, S. O. Valenzuela, M. Hanke and M. Ramsteiner, Large-area van der Waals epitaxy and magnetic characterization of Fe3GeTe2 films on graphene, *2D Mater.*, 2021, **8**, 041001.

13 R. Roemer, C. Liu and K. Zou, Robust ferromagnetism in wafer-scale monolayer and multilayer Fe3GeTe2, *npj 2D Mater. Appl.*, 2020, **4**, 33.

14 S. Liu, X. Yuan, Y. Zou, Y. Sheng, C. Huang, E. Zhang, J. Ling, Y. Liu, W. Wang, C. Zhang, J. Zou, K. Wang and F. Xiu, Wafer-scale two-dimensional ferromagnetic Fe3GeTe2 thin films grown by molecular beam epitaxy, *npj 2D Mater. Appl.*, 2017, **1**, 30.

15 H. Wang, Y. Liu, P. Wu, W. Hou, Y. Jiang, X. Li, C. Pandey, D. Chen, Q. Yang, H. Wang, D. Wei, N. Lei, W. Kang, L. Wen, T. Nie, W. Zhao and K. L. Wang, Above Room-Temperature Ferromagnetism in Wafer-Scale Two-Dimensional van der Waals Fe3GeTe2 Tailored by a Topological Insulator, *ACS Nano*, 2020, **14**(8), 10045–10053.

16 J. Seo, D. Y. Kim, E. S. An, K. Kim, G.-Y. Kim, S.-Y. Hwang, D. W. Kim, B. G. Jang, H. Kim, G. Eom, S. Y. Seo, R. Stania, M. Muntwiler, J. Lee, K. Watanabe, T. Taniguchi, Y. J. Jo, J. Lee, B. I. Min, M. H. Jo, H. W. Yeom, S.-Y. Choi, J. H. Shim and J. S. Kim, Nearly room temperature ferromagnetism in a magnetic metal-rich van der Waals metal, *Sci. Adv.*, 2020, **6**, eaay8912.

17 T. T. Ly, J. Park, K. Kim, H.-B. Ahn, N. J. Lee, K. Kim, T.-E. Park, G. Duvjir, N. H. Lam, K. Jang, C.-Y. You, Y. Jo, S. K. Kim, C. Lee, S. Kim and J. Kim, Direct Observation of Fe-Ge Ordering in Fe5−xGeTe2 Crystals and Resultant Helimagnetism, *Adv. Funct. Mater.*, 2021, **31**, 2009758.

18 J. Stahl, E. Shlaen and D. Johrendt, The van der Waals Ferromagnets Fe5−δGeTe2 and Fe5−δ−xNixGeTe2 – Crystal Structure; Stacking Faults and Magnetic Properties, *Z. Anorg. Allg. Chem.*, 2018, **644**, 1923–1929.

19 M. Ribeiro, G. Gentile, A. Marty, D. Dosenovic, H. Okuno, C. Vergnaud, J.-F. Jacquot, D. Jalabert, D. Longo, P. Ohresser, A. Hallal, M. Chshiev, O. Boulle, F. Bonell and M. Jamet, Large-scale epitaxy of two-dimensional van der Waals room temperature ferromagnet Fe5GeTe2, *npj 2D Mater. Appl.*, 2022, **6**, 10.

20 K. Yamagami, Y. Fujisawa, B. Driesen, C. H. Hsu, K. Kawaguchi, H. Tanaka, T. Kondo, Y. Zhang, H. Wadati, K. Araki, T. Takeda, Y. Takeda, T. Muro, F. C. Chuang, Y. Niimi, K. Kuroda, M. Kobayashi and Y. Okada, Itinerant ferromagnetism mediated by giant spin polarization of the metallic ligand band in the van der Waals magnet Fe5GeTe2, *Phys. Rev. B*, 2021, **103**, L060403.

21 H. Zhang, R. Chen, K. Zhai, X. Chen, L. Caretta, X. Huang, R. V. Chopdekar, J. Cao, J. Sun, J. Yao, R. Birgeneau and R. Ramesh, Itinerant ferromagnetism in van der Waals Fe5-xGeTe2 crystals above room temperature, *Phys. Rev. B*, 2020, **102**, 064417.

22 H. Chen, S. Asif, M. Whalen, J. Támara-Isaza, B. Luetke, Y. Wang, X. Wang, M. Ayako, S. Lamsal, A. F. May, M. A. McGuire, C. Chakraborty, J. Q. Xiao and M. J. H. Ku, Revealing room temperature ferromagnetism in exfoliated Fe5GeTe2 flakes with quantum magnetic imaging, *2D Mater.*, 2022, **9**, 025017.

23 G. K. R. Nair, Z. Zhang, F. Hou, A. Abdelaziem, X. Xu, S. W. Q. Yang, N. Zhang, W. Li, C. Zhu, Y. Wu, H. Weiling, L. Kang, T. Salim, J. Zhou, L. Ke, J. Lin, X. Li, W. Gao and Z. Liu, Phase-pure two-dimensional FexGeTe2 magnets with near-room temperature TC, *Nano Res.*, 2022, **15**, 457–464.

24 C. Tan, W.-Q. Xie, G. Zheng, N. Aloufi, S. Albarakati, M. Algarni, J. Li, J. Partridge, D. Culcer, X. Wang, J. B. Yi, M. Tian, Y. Xiong, Y.-J. Zhao and L. Wang, Gate-Controlled Magnetic Phase Transition in a van der Waals Magnet Fe5GeTe2, *Nano Lett.*, 2021, **21**(13), 5599–5605.

25 A. F. May, C. A. Bridges and M. A. McGuire, Physical properties and thermal stability of Fe5-xGeTe2 single crystals, *Phys. Rev. Mater.*, 2019, **3**, 104401.

26 A. F. May, D. Ovchinnikov, Q. Zheng, R. Hermann, S. Calder, B. Huang, Z. Fei, Y. Liu, X. Xu and M. A. McGuire, Ferromagnetism near room temperature in the cleavable van der Waals crystal Fe5GeTe2, *ACS Nano*, 2019, **13**, 4436–4442.

27 T. Ohta, K. Sakai, H. Taniguchi, B. Driesen, Y. Okada, K. Kobayashi and Y. Niimi, Enhancement of coercive field in atomically thin quenched Fe5GeTe2, *Appl. Phys. Express*, 2020, **13**, 043005.

28 Z. Li, W. Xia, H. Su, Z. Yu, Y. Fu, L. Chen, X. Wang, N. Yu, Z. Zou and Y. Guo, Magnetic critical behavior of the van der Waals Fe5GeTe2 crystal with near room temperature ferromagnetism, *Sci. Rep.*, 2020, **10**, 1–10.

29 L. Alahmed, B. Nepal, J. Macy, W. Zheng, B. Casas, A. Sapkota, N. Jones, A. R. M. Brahlek, W. Jin, M. Mahjouri-Samani, S. S.-L. Zhang, C. Mewes, L. Balicas, T. Mewes and P. Li, Magnetism and spin dynamics in room-temperature van der Waals magnet Fe5GeTe2, *2D Mater.*, 2021, **8**, 045030.

30 T. Ohta, M. Tokuda, S. Iwakiri, K. Sakai, B. Driesen, Y. Okada, K. Kobayashi and Y. Niimi, Butterfly-shaped magnetoresistance in van der Waals ferromagnet Fe5GeTe2, *AIP Adv.*, 2021, **11**, 025014.

31 A. F. May, J. Yan, R. Hermann, M.-H. Du and M. A. McGuire, Tuning the room temperature ferromagnetism in Fe5GeTe2 by arsenic substitution, *2D Mater.*, 2022, **9**, 015013.

32 A. F. May, M.-H. Du, V. R. Cooper and M. A. McGuire, Tuning magnetic order in the van der Waals metal Fe5GeTe2 by cobalt substitution, *Phys. Rev. Mater.*, 2020, **4**, 074008.

33 G. Kresse and J. Furthmüller, Efficient iterative schemes for ab initio total-energy calculations using a plane-wave basis set, *Phys. Rev. B: Condens. Matter Mater. Phys.*, 1996, **54**(16), 11169–11186.

34 G. Kresse and D. Joubert, From ultrasoft pseudopotentials to the projector augmented-wave method, *Phys. Rev. B: Condens. Matter Mater. Phys.*, 1999, **59**(3), 1758–1775.

35 J. P. Perdew, K. Burke and M. Ernzerhof, Generalized Gradient Approximation Made Simple, *Phys. Rev. Lett.*, 1996, **77**(18), 3865–3868.

36 D. J. Chadi and M. L. Cohen, Special Points in the Brillouin Zone, *Phys. Rev. B: Solid State*, 1973, **8**(12), 5747–5753.

37 P. E. Blöchl, O. Jepsen and O. K. Andersen, Improved tetrahedron method for Brillouin-zone integrations, *Phys. Rev. B: Condens. Matter Mater. Phys.*, 1994, **49**(23), 16223–16233.

38 S. Grimme, J. Antony, S. Ehrlich and H. Krieg, A consistent and accurate ab initio parametrization of density functional dispersion correction (DFT-D) for the 94 elements H-Pu, *J. Chem. Phys.*, 2010, **132**, 154104.

39 E. Longo, L. Locatelli, M. Belli, M. Alia, A. Kumar, M. Longo, M. Fanciulli and R. Mantovan, Spin–Charge Conversion in Fe/Au/Sb2Te3 Heterostructures as Probed By Spin Pumping Ferromagnetic Resonance, *Adv. Mater. Interfaces*, 2021, **8**, 2101244.

40 E. Longo, M. Belli, M. Alia, M. Rimoldi, R. Cecchini, M. Longo, C. Wiemer, L. Locatelli, P. Tsipas, A. Dimoulas, G. Gubbiotti, M. Fanciulli and R. Mantovan, Large Spin-to-Charge Conversion at Room Temperature in Extended Epitaxial Sb2Te3 Topological Insulator Chemically Grown on Silicon, *Adv. Funct. Mater.*, 2021, **32**, 2109361.

41 S. Ershadrad, S. Ghosh, D. Wang, Y. Kvashnin and B. Sanyal, Unusual Magnetic Features in Two-Dimensional Fe5GeTe2 Induced by Structural Reconstructions, *J. Phys. Chem. Lett.*, 2022, **13**(22), 4877–4883.

42 B. Liu, S. Liu, L. Yang, Z. Chen, E. Zhang, Z. Li, J. Wu, X. Ruan, F. Xiu, W. Liu, L. He, R. Zhang and Y. Xu, Light-Tunable Ferromagnetism in Atomically Thin Fe3GeTe2 Driven by Femtosecond Laser Pulse, *Phys. Rev. Lett.*, 2020, **125**, 267205.

43 M. Joe, U. Yang and C. Lee, First-principles study of ferromagnetic metal Fe5GeTe2, *Nano Mater. Sci.*, 2019, **1**, 299–303.

44 M. Farle, Ferromagnetic Resonance of Ultrathin Metallic Layers, *Rep. Prog. Phys.*, 1998, **61**(7), 755–826.

45 E. Montoya, T. McKinnon, A. Zamani, E. Girt and B. Heinrich, Broadband Ferromagnetic Resonance System and Methods for Ultrathin Magnetic Films, *J. Magn. Magn. Mater.*, 2014, **356**, 12–20.

46 Y. Tserkovnyak, A. Brataas and G. E. W. Bauer, Enhanced Gilbert Damping in Thin Ferromagnetic Films, *Phys. Rev. Lett.*, 2002, **88**(11), 4.

47 S. Maekawa, S. O. Valenzuela, E. Saitoh and T. Kimura, *Spin Current*, Oxford University Press, Oxford, 2012.

48 M. Dc, T. Liu, J. Y. Chen, T. Peterson, P. Sahu, H. Li, Z. Zhao, M. Wu and J. P. Wang, Room-Temperature Spin-to-Charge Conversion in Sputtered Bismuth Selenide Thin Films via Spin Pumping from Yttrium Iron Garnet, *Appl. Phys. Lett.*, 2019, **114**, 10.

49 F. B. Abdulahad, J. H. Lin, Y. Liou, W. K. Chiu, L. J. Chang, M. Y. Kao, J. Z. Liang, D. S. Hung and S. F. Lee, Spin Chemical Potential Bias Induced Surface Current Evidenced by Spin Pumping into the Topological Insulator Bi2Te3, *Phys. Rev. B: Condens. Matter Mater. Phys.*, 2015, **92**, 2.